Intrafractional tracking accuracy in infrared marker-based hybrid dynamic tumour-tracking irradiation with a gimballed linac

Nobutaka Mukumoto[a], Mitsuhiro Nakamura[a,*], Masahiro Yamada[a], Kunio Takahashi[b], Hiroaki Tanabe[c], Shinsuke Yano[d], Yuki Miyabe[a], Nami Ueki[a], Shuji Kaneko[a], Yukinori Matsuo[a], Takashi Mizowaki[a], Akira Sawada[a,e], Masaki Kokubo[c,f], and Masahiro Hiraoka[a]

[a] Department of Radiation Oncology and Image-applied Therapy, Graduate School of Medicine, Kyoto University, Kyoto, Japan

[b] Advanced Mechanical Systems Department, Mitsubishi Heavy Industries Ltd, Hiroshima, Japan

[c] Division of Radiation Oncology, Institute of Biomedical Research and Innovation, Hyogo, Japan

[d] Division of Clinical Radiology Service, Kyoto University Hospital, Kyoto, Japan

[e] Department of Radiological Technology, Faculty of Medical Science, Kyoto College of Medical Science, Kyoto, Japan

[f] Department of Radiation Oncology, Kobe City Medical Center General Hospital, Hyogo, Japan

*** Corresponding author:** Mitsuhiro Nakamura, Ph.D., Graduate School of Medicine, Kyoto University, 54 Kawahara-cho, Shogoin, Sakyo-ku, Kyoto, 606-8507, Japan.
Tel.: +81-75-751-3762; Fax: +81-75-771-9749; E-mail: m_nkmr@kuhp.kyoto-u.ac.jp

Total number of pages: 16 **(Tables**: 2; **Figures**: 2; **Supplementary Material**: 1)

Running title: Intrafractional accuracy of IR Tracking

Key words: Four-dimensional image-guided radiotherapy, dynamic tumour-tracking irradiation, respiratory motion, Vero4DRT, intra-fractional tracking accuracy.

Meeting presentation: This work was accepted for presentation during the poster viewing session of the 54th Annual Meeting of the American Society for Radiation Oncology in Boston, October 28-31, 2012.

ABSTRACT

Purpose: To verify the intrafractional tracking accuracy in infrared (IR) marker-based hybrid dynamic tumour tracking irradiation ("IR Tracking") with the Vero4DRT.

Materials and Methods: The gimballed x-ray head tracks a moving target by predicting its future position from displacements of IR markers in real-time. Ten lung cancer patients who underwent IR Tracking were enrolled. The 95th percentiles of intrafractional mechanical (iE_M^{95}), prediction (iE_P^{95}), and overall targeting errors (iE_T^{95}) were calculated from orthogonal fluoroscopy images acquired during tracking irradiation and from the synchronously acquired log files.

Results: Averaged intrafractional errors were (left-right, cranio-caudal [CC], anterior-posterior [AP]) = (0.1 mm, 0.4 mm, 0.1 mm) for iE_M^{95}, (1.2 mm, 2.7 mm, 2.1 mm) for iE_P^{95}, and (1.3 mm, 2.4 mm, 1.4 mm) for iE_T^{95}. By correcting systematic prediction errors in the previous field, the iE_P^{95} was reduced significantly, by an average of 0.4 mm in the CC ($p < 0.05$) and by 0.3 mm in the AP ($p < 0.01$) directions.

Conclusions: Prediction errors were the primary cause of overall targeting errors, whereas mechanical errors were negligible. Furthermore, improvement of the prediction accuracy could be achieved by correcting systematic prediction errors in the previous field.

INTRODUCTION

Respiratory motion is one of the factors causing uncertainties during beam delivery, particularly for thoracic and abdominal tumours [1, 2]. In hypofractionated stereotactic body radiotherapy for lung cancer patients, addition of a large margin to compensate for respiratory motion increases the probability of complications [3]. Several techniques, including forced shallow-breathing, breath-hold, respiratory gating, and dynamic tumour tracking (DTT), have been proposed to reduce the uncertainties caused by respiratory motion [1, 2]. Of these methods, recent interest has focused on the DTT technique, which can reposition the radiation beam dynamically in accordance with the target position. DTT can minimise the internal uncertainties without a burden on the respiration of patients or prolongation of treatment time.

We have developed an innovative four-dimensional (4D) image-guided radiotherapy system, the Vero4DRT (MHI-TM2000; Mitsubishi Heavy Industries, Ltd., Japan, and BrainLAB, Feldkirchen, Germany) [4-10], and used its hybrid DTT irradiation function [infrared (IR)-marker-based hybrid DTT irradiation ("IR Tracking")] clinically in lung cancer patients since September 2011 [10]. In IR Tracking, the position of the target, indicated by implanted fiducial markers, is calculated from external surrogate signals through a pre-built prediction model ("4D model"), and the MV x-ray beam is delivered with real-time monitoring [7, 8, 10-12]. Depuydt et al. showed that the performance of Vero4DRT's DTT function was comparable with other clinical DTT systems in phantom and patient simulation studies [11, 12]. Our group also previously revealed that the accuracy of the 4D model must be verified before treatment, and margins were required to compensate for the prediction error in a phantom study [7]; it was concluded that the accuracy of the 4D model was affected by the baseline drift of respiratory motion [8]. Here, we verified the intrafractional tracking accuracy of IR Tracking for lung cancer patients using intrafractional monitoring images and the corresponding log files.

MATERIALS AND METHODS

The Vero4DRT hybrid dynamic tumour tracking irradiation system

Supplementary Figure 1 (Electronic Appendix) shows a schematic diagram of the Vero4DRT system. The Vero4DRT has several unique components that facilitate DTT irradiation: (1) a compact C-band 6-MV x-ray head with a gimbal mechanism, mounted on an O-ring gantry. The gimballed x-ray head can swing itself in both the pan and tilt directions, (2) gantry-mounted orthogonal kV x-ray imaging subsystems, consisting of two sets of x-ray tubes and flat-panel detectors, with a spatial resolution of 0.2 mm at the isocentre level, and (3) an extended version of the ExacTRAC system that enables real-time motion monitoring and management for the DTT function [7, 8, 11, 12] with an IR camera mounted on the ceiling of the treatment room.

Supplementary Figure 2 shows a schematic diagram of the IR Tracking procedure. After patient positioning, a 4D model is created using synchronously monitored internal target motion and an external surrogate signal. The detected target position (P_d) is defined as the tumour centre-of-mass calculated from the positions of the implanted fiducial markers on the x-ray images. The relative shift amount between the tumour centre-of-mass and centroid of the markers' polyhedron was determined at the end-exhalation phase in the planning computed tomography. The predicted target position (P_p) is calculated from the 4D model, expressed by a quadratic equation involving two variables, the position and velocity of the IR markers. The positions of the IR markers are predicted linearly from the past motion to compensate for the DTT system delay [11]. Details of the prediction model are described in the Supplementary Materials section. In this 4D-modelling phase, the peak-to-peak amplitude of the detected target motion (A) and the mean (μ) and standard deviation (SD) of the absolute 4D-modelling error (E_{4DM}), defined as the absolute difference between the P_p and P_d, are calculated along each axis automatically. During beam delivery, the future 3D target position is calculated from the displacements of the IR markers using the 4D model, and then the corresponding tracking angle is transferred continuously to the gimballed x-ray head. Additionally, circles with a user-defined radius around the predicted positions of the fiducial markers (tolerance circles) are displayed on the monitoring images as a benchmark in re-modelling. When the fiducial markers are deviated systematically from the tolerance circles, re-modelling should be performed during each treatment session (Fig. 1).

Patient characteristics and treatment planning

Ten lung cancer patients who underwent IR Tracking in an Institutional Review Board-approved trial were included in the present study. Patient selection criteria were based on our stereotactic body radiation therapy protocol and written informed consent for the present study was obtained from each patient [3, 10]. Three or more 1.5-mm-diameter gold markers (Olympus Co., Tokyo, Japan) were implanted around the lung tumour transbronchially 1–2 weeks before treatment planning. Table 1 shows the characteristics of the patients and treatment planning. We performed a dry-run treatment session prior to treatment planning to assess the characteristics of respirations and to identify patient-specific planning target volume (PTV) margins [7, 9]. The median of A was 2.8 mm in the left-right (LR), 15.8 mm in the cranio-caudal (CC), and 4.3 mm in the anterior-posterior (AP) directions. The median of μ+2SD of the E_{4DM} during the dry-run treatment session ($E_{4DM}^{\mu+2SD}$) was 0.6 mm in the LR, 1.9 mm in the CC, and 0.7 mm in the AP directions. Patient-specific PTV margins of 5.0–9.0 mm were added to the tumour along each axis to compensate for intra- and interfractional uncertainties in IR Tracking [7, 9, 13]. Supplementary Figure 3 shows the definition of the patient-specific PTV margins. The intra- and interfractional uncertainties were classified into systematic and random components. The patient-specific PTV margins were then calculated for each axis using the formula in Supplementary Figure 3. Prescribed doses of 48 or 56 Gy were specified to isocentre in four fractions. Treatment plans included 6-8 non-coplanar fields, with a dose rate of 500 MU/min.

Data acquisition during beam delivery

During beam delivery, the target and fiducial markers were monitored using orthogonal kV x-ray imaging subsystems at 1 Hz. The predicted target positions and tracking angles of the gimballed x-ray head were recorded in log files at 60 and 200 Hz, respectively. In total, 9268 paired images (~30 paired images per field) and corresponding log files were acquired.

Verification of intrafractional tracking accuracy

Intrafractional tracking accuracy was verified by the P_d from the fluoroscopic images and the corresponding P_p and the tracked target position, calculated from the synchronously acquired log files. Supplementary Figure 4 shows the geometric point of the tracked target position at the depth of the P_d ($P_{t,d}$). The tracked target position at the depth of the P_p ($P_{t,p}$), was calculated similarly. Intrafractional mechanical (iE_M), prediction (iE_P), and overall targeting errors (iE_T) were defined as the differences between $P_{t,p}$ and P_p, P_p and P_d, and $P_{t,d}$ and P_d, respectively. Details of the calculation process are described in the Supplementary Materials section.

The 95th percentiles of the absolute iE_M (iE_M^{95}), iE_P (iE_P^{95}), and iE_T (iE_T^{95}) during the treatment course were then calculated using the intrafractional monitoring images and the corresponding log files. Pearson correlation coefficients were calculated to assess the relationship between $E_{4DM}^{\mu+2SD}$ during the dry-run treatment session and iE_P^{95} or iE_T^{95} during the treatment course. To further improve the prediction accuracy, the corrected iE_P^{95} was recalculated retrospectively by subtracting the systematic (*i.e.* signed overall mean) iE_P in the previous field excluding the first field after the 4D modelling. A paired *t*-test with a 0.05 significance level was performed for statistical analysis.

RESULTS

Table 2 summarises iE_M^{95}, iE_P^{95}, iE_T^{95}, and corrected iE_P^{95} for 10 lung cancer patients.

Averaged intrafractional tracking errors were (LR, CC, AP) = (0.1 mm, 0.4 mm, 0.1 mm) for iE_M^{95}, (1.2 mm, 2.7 mm, 2.1 mm) for iE_P^{95}, and (1.3 mm, 2.4 mm, 1.4 mm) for iE_T^{95}. Additionally, a strong positive correlation was found between $E_{4DM}^{\mu+2SD}$ and iE_P^{95} (LR, CC, AP) = (0.73 [p = 0.017], 0.82 [p = 0.003], 0.96 [p = 0.000]) or iE_T^{95} (LR, CC, AP) = (0.69 [p = 0.028], 0.77 [p = 0.010], 0.90 [p = 0.001]). As shown in Table 2, iE_P^{95} was the primary cause of iE_T^{95}, while iE_M^{95} was negligible. The iE_T^{95} was fully covered by the PTV margin, including the geometric variations between the tumour and fiducial markers. Figure 2 (a) shows representative probability histograms in the positional error in the CC direction for the first patient who underwent IR Tracking (Patient No. 1). iE_T^{95} was 2.3 mm for this patient.

A maximum iE_T^{95} of 4.1 mm was observed for Patient No. 7 in the CC direction. This patient showed the largest difference between $E_{4DM}^{\mu+2SD}$ and iE_P^{95} [LR, CC, and AP = 1.6, 1.5, and 1.6 mm, respectively] due to a baseline drift during beam delivery. Meanwhile, the averaged differences for the other patients were 0.3, 0.6, and 0.7 mm for the LR, CC, and AP directions, respectively. By correcting the systematic prediction errors in the previous field, however, iE_P^{95} decreased, from 4.1 to 2.7 mm, for this patient in the CC direction [Fig. 2 (b)]. The maximum reductions in iE_P^{95} were observed in this patient (LR, CC, AP) = (1.4 mm, 1.4 mm, 0.9 mm). For the entire population, the corrected iE_P^{95} was improved significantly by an average of 0.4 mm in the CC ($p < 0.05$) and by 0.3 mm in the AP ($p < 0.01$) directions.

DISCUSSION

The Vero4DRT tracks a moving target in real-time using the orthogonal gimballed x-ray head. In the present study, we established a verification methodology for the intrafractional mechanical, prediction, and overall targeting accuracy in each axis during the treatment course. The 3D coordinates of the intrafractional tracked target position were calculated based on the MV x-ray beam orientation using intrafractional monitoring images and the corresponding log files.

We verified the intrafractional tracking accuracy for 10 lung cancer patients who underwent IR Tracking with real-time monitoring. Vero4DRT users can monitor the moving target, fiducial markers, and tolerance circles with its predicted position using orthogonal kV x-ray imaging subsystems during beam delivery. At our institution, the radius of the tolerance circles is set to 3 mm, and the 4D model is re-modelled when the monitored fiducial markers' positions are displaced systematically from the tolerance circles due to baseline drift (Fig. 1). By re-modelling the 4D model, while an iE_T^{95} of less than 3 mm was achieved for nine patients (90%), one patient (Patient No. 7) showed a large iE_T^{95} of greater than 3 mm. The 4D model was updated once during the treatment session for Patient No. 7. However, this patient required additional re-modelling. In IR Tracking, the predominant cause of overall targeting errors was prediction errors. The position and velocity of IR markers involved in the 4D model were predicted linearly from past IR marker motion [8]. Thus, prediction uncertainty of the peak position sometimes overestimated the predicted position of the IR marker and the 4D model enforced a large amplitude of respiration motion (Supplementary Figure 5). In this case, the mechanical response delay of the gimballed x-ray head reduced the impact of the prediction error on the overall targeting error. Thus, the overall targeting errors were sometimes smaller than the prediction errors. Additionally, there were strong correlations between $E_{4DM}^{\mu+2SD}$ and iE_{P}^{95} or iE_{T}^{95}, indicating that intrafractional prediction or overall targeting errors during the treatment course could be estimated from 4D modelling errors during the dry-run treatment session. The iE_{T}^{95} was fully covered by the PTV margin, including a geometric variation between the tumour and fiducial markers of 2.5 mm (Tables 1 and 2). When calculating the PTV margin in IR Tracking, the intra- and interfractional uncertainties should be considered (Supplementary Figure 3). However, the present recipe of the patient-specific PTV margin was tentative so as to perform IR Tracking safely. Therefore, further investigations will be needed to determine the PTV margin size appropriate for IR Tracking [9].

The CyberKnife Robotic Radiosurgery System with the integrated Synchrony Respiratory Tracking System (Accuray, Sunnyvale, CA) substantially reduces the geometric error caused by respiratory motion [14, 15]. In the present study, $E_{4DM}^{\mu+2SD}$ was comparable with results of the Synchrony system. However, the correlation between the internal target positions and external surrogates can change in the presence of baseline drift, reducing the accuracy of the prediction model [8, 16]. The Synchrony system periodically updates the prediction model using the intrafractional monitoring images. Updating the 4D model in real-time may also improve the prediction accuracy because the internal/external correlation change or baseline drift in respiration will be corrected. Meanwhile, this is difficult regarding image processing time and minimum interval of the x-ray acquisition during beam delivery. The 4D model in IR Tracking includes the parameters of position and velocity of the IR markers. To update the 4D model, these parameters must be changed. Thus, a shorter monitoring interval would be necessary. In clinical practice, we re-modelled the 4D model at least once during treatment to minimise intrafractional uncertainties due to internal/external correlation change or baseline drift in respiration. However, re-modelling required additional exposures that were 8.3-16.7 times higher than intrafractional monitoring [4, 12]. Also, x-ray image-based DTT, another DTT approach with Vero4DRT [6], would not be an alternative strategy in terms of the difficulty of real-time detection and excessive imaging doses. In the current study, the overall mean errors of iE_P were calculated from around 30 paired images retrieved in the previous field using the monitoring function for the intrafractional tracking accuracy verification. Because the systematic prediction errors resulting from the baseline drift of respiration were reduced by subtracting the overall mean errors of iE_P in the previous field, iE_P^{95} decreased significantly in the CC and AP directions using the monitoring images during beam delivery. In the current study, we used all monitoring images to calculate the systematic prediction errors because iE_P varied according to the respiratory phase. However, a triggered x-ray acquisition based on the respiratory phase would also reduce iE_P^{95} using a small number of monitoring images because the systematic prediction errors could be corrected by the averaged iE_P at the end-expiratory and end-inspiratory phases.

CONCLUSIONS

We demonstrated that IR Tracking reduced the impact of respiratory motion substantially. The prediction error was the primary cause of the overall targeting error, while the mechanical error was negligible. The PTV margin fully covered the intrafractional overall targeting errors. The 4D modelling errors during a dry-run treatment session were a good indicator of the prediction and overall targeting errors during the treatment course. Additionally, further improvement in prediction accuracy was achieved by correcting the systematic prediction error in the previous field.

CONFLICTS OF INTEREST STATEMENT

This research was sponsored in part by Mitsubishi Heavy Industries, Ltd., Japan. Takashi Mizowaki, Masaki Kokubo, and Masahiro Hiraoka have consultancy agreements with Mitsubishi Heavy Industries, Ltd.

ACKNOWLEDGEMENTS

This research was supported by the Japan Society for the Promotion of Science (JSPS) through its “Funding Program for World-Leading Innovative R&D on Science and Technology (FIRST Program).”

REFERENCES

[1] Keall P J, Mageras G S, Balter J M, *et al*. The management of respiratory motion in radiation oncology report of AAPM task group 76. Med Phys 2006;33:3874–900.

[2] Korreman S S. Motion in radiotherapy: photon therapy. Phys Med Biol 2012;57:R161–91.

[3] Matsuo Y, Shibuya K, Nakamura M, *et al*. Dose-volume metrics associated with radiation pneumonitis after stereotactic body radiation therapy for lung cancer. Int J Radiat Oncol Biol Phys 2012;83:e545–9.

[4] Kamino Y, Takayama K, Kokubo M, *et al*. Development of a four-dimensional image-guided radiotherapy system with a gimbaled X-ray head. Int J Radiat Oncol Biol Phys 2006;66:271–8.

[5] Takayama K, Mizowaki T, Kokubo M, *et al*. Initial validations for pursuing irradiation using a gimbals tracking system. Radiother Oncol 2009;93:45–9.

[6] Mukumoto N, Nakamura M, Sawada A, *et al*. Positional accuracy of novel x-ray-image-based dynamic tumor-tracking irradiation using a gimbaled MV x-ray head of a Vero4DRT (MHI-TM2000). Med Phys 2012;39:6287–96.

[7] Mukumoto N, Nakamura M, Sawada A, *et al*. Accuracy verification of infrared marker-based dynamic tumor-tracking irradiation using the gimbaled x-ray head of the Vero4DRT (MHI-TM2000). Med Phys 2013;40:041706-1–9.

[8] Akimoto M, Nakamura M, Mukumoto N, *et al*. Predictive uncertainty in infrared marker-based dynamic tumor tracking with Vero4DRT. Med Phys 2013;40:091705 -1–8.

[9] Nakamura M, Mukumoto N, Ueki N, *et al*. Estimation of a tracking margin in surrogate signal-based dynamic tumor tracking irradiation with Vero4DRT. Int J Radiat Oncol Biol Phys 2012;84:S851–2.

[10] Matsuo Y, Sawada A, Ueki N, *et al*. An initial experience of dynamic tumor tracking irradiation with real-time monitoring using Vero4DRT (MHI-TM2000). Radiother Oncol 2012;103:S64.

[11] Depuydt T, Verellen D, Haas O, *et al*. Geometric accuracy of a novel gimbals based radiation therapy tumor tracking system. Radiother Oncol 2011;98:365-72.

[12] Depuydt T, Poelsa K, Verellen D, *et al*. Initial assessment of tumor tracking with a gimbaled linac system in clinical circumstances: A patient simulation study. Radiother Oncol 2013;106:236–40.

[13] Ueki N, Matsuo Y, Nakamura M, *et al*. Intra- and interfractional variations in geometric arrangement between lung tumours and implanted markers. Radiother Oncol 2013, in press.

[14] Hoogeman M, Prévost J B, Nuyttens J, *et al*. Clinical accuracy of the respiratory tumor tracking system of the cyberknife: assessment by analysis of log files. Int J Radiat Oncol Biol Phys 2009;74:297–303.

[15] Pepin E W, Wu H, Zhang Y, *et al*. Correlation and prediction uncertainties in the cyberknife synchrony respiratory tracking system. Med Phys 2011;38:4036-44.

[16] Malinowski K, McAvoy T J, George R, *et al*. Incidence of changes in respiration-induced tumor motion and its relationship with respiratory surrogates during individual treatment fractions. Int J Radiat Oncol Biol Phys 2012;82:1665–73.

FIGURE LEGENDS

Figure 1. Screen shot of the Vero4DRT during infrared (IR)-marker-based DTT irradiation ("IR Tracking"). Monitored fiducial markers' positions were located outside of the "Tolerance circle" displayed around the predicted fiducial markers' positions due to the baseline drift of respiration.

Figure 2. Probability histograms of positional errors in the cranio-caudal (CC) direction (a) for the first patient who underwent IR Tracking (Patient No. 1) and (b) for the most improved patient with intrafractional prediction error (iE_P) correction (Patient No. 7). The Vero4DRT reduced the motion blurring effect caused by respiration.

TABLES

Table 1. Characteristics of the patients and treatment planning.

Patient no.	Age (y.o.)	Sex	Tumour stage	Tumour side	Tumour location	A [mm]			$E_{4DM}^{\mu+2SD}$ [mm]			GTV [cc]	PTV margin [mm]			PTV [cc]
						LR	CC	AP	LR	CC	AP		LR	CC	AP	
1	85	F	Metastasis	Rt	S6	2.2	14.8	2.2	0.2	1.4	0.6	38.7	5.0	7.0	5.0	87.0
2	82	M	T1a	Rt	S9	4.6	19.8	4.4	1.6	3.3	0.5	11.0	5.0	8.0	5.0	34.6
3	86	F	T1b	Rt	S9	2.2	26.0	5.3	0.2	1.6	0.8	12.4	5.0	8.0	5.0	38.0
4	84	M	T1b	Rt	S6	0.9	11.9	3.1	0.3	1.3	0.7	17.8	5.0	7.0	5.0	50.1
5	71	M	T1b	Rt	S5	7.4	3.4	5.1	1.3	1.0	0.7	12.5	5.0	5.0	5.0	33.6
6	87	M	T1b	Lt	S8	2.9	29.6	15.5	0.6	2.2	3.9	20.6	5.0	8.0	8.0	64.1
7	61	M	T2a	Rt	S10	1.4	8.8	4.0	0.5	2.6	0.7	31.9	5.0	6.5	5.0	74.2
8	85	M	T1a	Lt	S9	5.8	30.6	8.7	2.1	3.4	2.9	8.9	5.0	9.0	6.0	33.4
9	68	M	Metastasis	Lt	S8	2.7	9.9	2.3	0.2	0.9	0.4	2.3	5.0	5.0	5.0	10.4
10	60	M	Metastasis	Rt	S9	3.1	16.7	4.1	0.9	2.2	1.6	13.3	5.0	7.0	5.0	38.9

Abbreviations: A=peak-to-peak amplitude of respiration, $E_{4DM}^{\mu+2SD}$= mean plus two standard deviations of the absolute 4D-modelling error during a dry-run treatment session, GTV=gross tumour volume, PTV=planning target volume, LR=left-right, CC=cranio-caudal, AP=anterior-posterior, F=Female, M=Male, Rt=Right lobe, Lt=Left lobe, S= pulmonary segment.

Table 2. iE_M^{95}, iE_P^{95}, iE_T^{95}, and corrected iE_P^{95}.

Patient no.	iE_M^{95} [mm]			iE_P^{95} [mm]			iE_T^{95} [mm]			Corrected iE_P^{95} [mm]		
	LR	CC	AP	LR	CC	AP	LR	CC	AP	LR	CC	AP
1	0.1	0.3	0.1	0.6	2.7	1.3	0.9	2.3	1.0	0.6	1.9	1.2
2	0.3	0.7	0.2	1.4	3.4	0.8	1.3	3.0	0.7	1.3	3.1	0.6
3	0.1	0.4	0.1	0.7	2.5	1.5	0.8	2.2	1.0	0.7	2.7	1.3
4	0.1	0.4	0.1	0.8	2.0	1.5	0.8	1.7	1.0	0.8	1.7	1.4
5	0.1	0.1	0.1	1.8	1.5	1.6	1.1	1.5	1.2	1.5	1.5	1.6
6	0.1	0.3	0.1	1.0	2.5	5.0	1.9	2.3	2.9	0.9	1.8	4.3
7	0.2	0.8	0.2	2.1	4.1	2.3	1.4	4.1	1.6	0.7	2.7	1.4
8	0.2	0.4	0.1	2.1	3.2	3.4	2.2	2.8	1.6	2.5	3.2	3.2
9	0.1	0.3	0.1	0.5	1.6	1.4	0.8	1.4	0.9	0.4	1.3	1.1
10	0.1	0.3	0.1	1.1	3.0	2.0	1.3	2.9	1.6	1.0	2.7	1.8
Average	0.1	0.4	0.1	1.2	2.7	2.1	1.3	2.4	1.4	1.0	2.3	1.8

Abbreviations: iE_M^{95} =95th percentiles of the absolute intrafractional mechanical error, iE_P^{95} =95th percentiles of the absolute intrafractional prediction error, iE_T^{95} =95th percentiles of the absolute intrafractional overall targeting error, LR=left-right, CC=cranio-caudal, AP=anterior-posterior.

Figure 1
Click here to download high resolution image

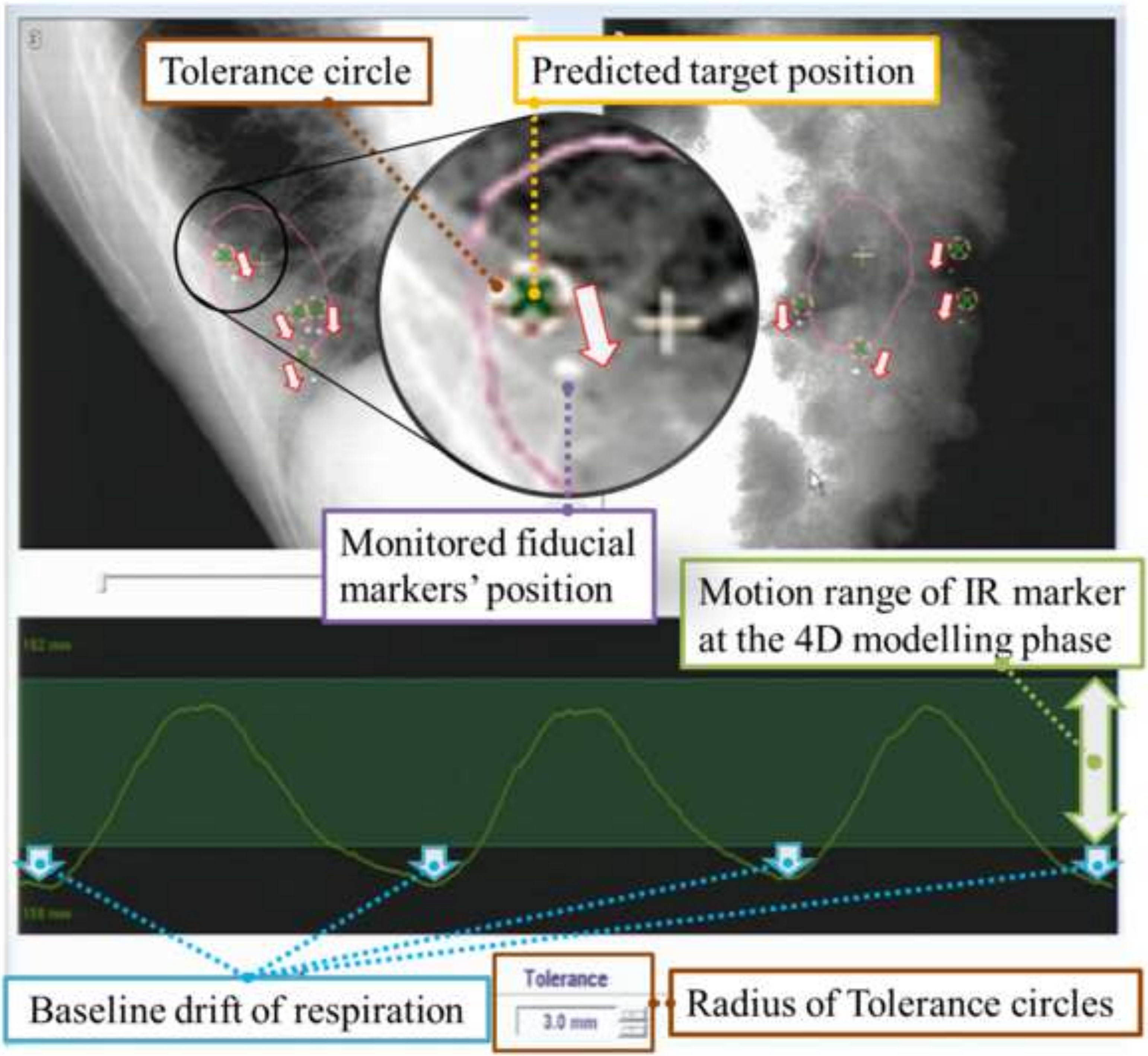

Figure 2
Click here to download high resolution image

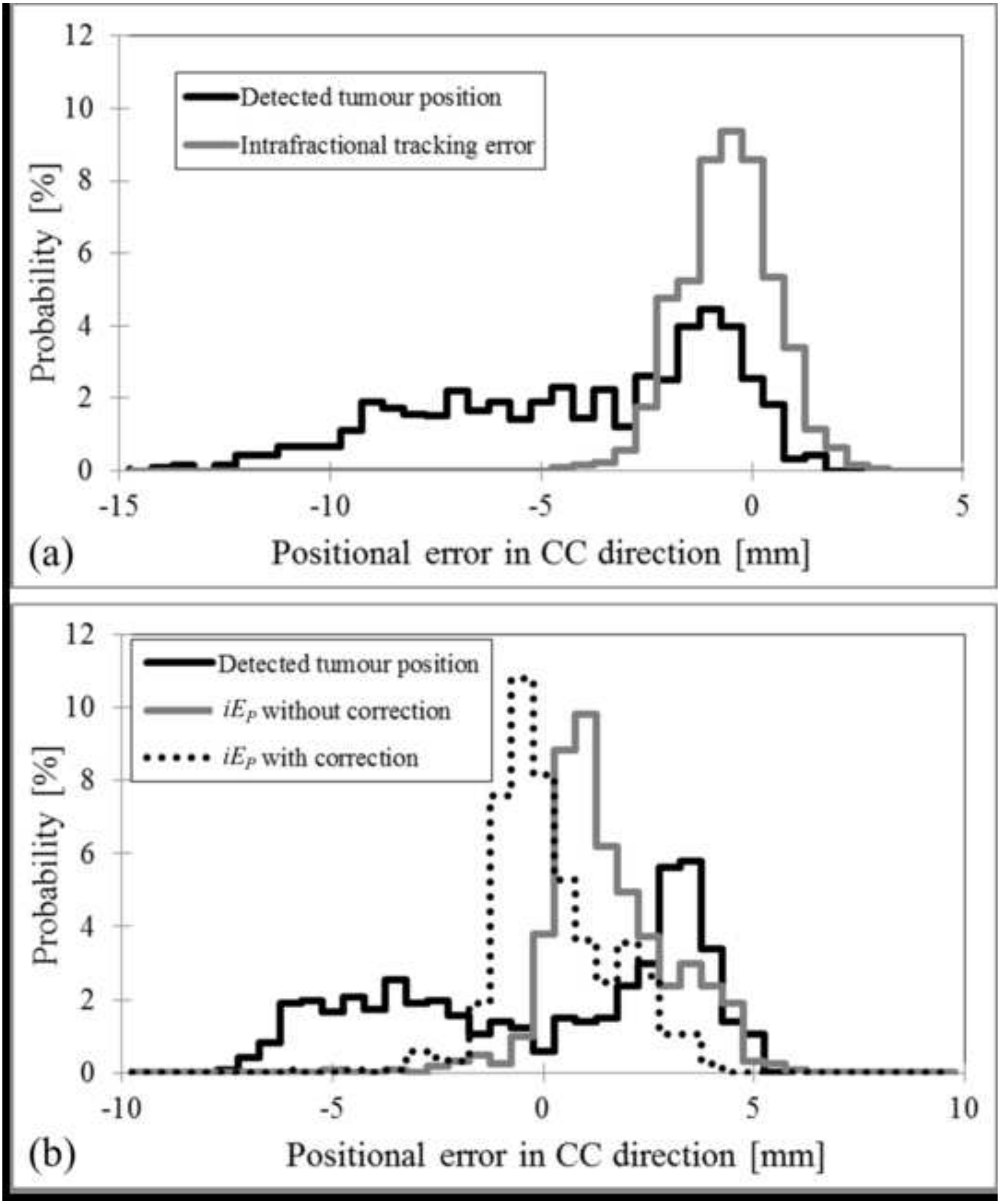

Prediction model of the Vero4DRT

Before irradiation, a prediction model ("4D model") was created. Infrared (IR) marker displacements and the implanted fiducial markers' motions were monitored for 20-40 s using the IR camera of the ExacTRAC system every 16.7 ms and the orthogonal kV x-ray imaging subsystems every 80 or 160 ms, respectively. The frame rate of x-ray monitoring changed automatically depending on IR marker velocity.

After monitoring, two target positions are determined: the detected target position (P_d) and the predicted target position (P_p). The P_d is defined as the tumour centre-of-mass calculated from the positions of the implanted fiducial markers on the x-ray images. The relative shift amount between the tumour centre-of-mass and centroid of the markers' polyhedron was determined at the end-exhalation phase in the planning computed tomography. The positions of the implanted fiducial markers were detected automatically based on the intensity ratios of the fiducial markers to their surroundings with an accuracy of 0.2 mm. The P_p is calculated from the predicted position and velocity of IR markers using the 4D model, expressed as follows:

$$P_p = \begin{pmatrix} x_p \\ y_p \\ z_p \end{pmatrix} = \frac{1}{n} \begin{pmatrix} \sum_{i=1}^{n} (a_{x,i} s_i^2 + b_{x,i} s_i + c_{x,i} + d_{x,i} v_i^2 + e_{x,i} v_i) \\ \sum_{i=1}^{n} (a_{y,i} s_i^2 + b_{y,i} s_i + c_{y,i} + d_{y,i} v_i^2 + e_{y,i} v_i) \\ \sum_{i=1}^{n} (a_{z,i} s_i^2 + b_{z,i} s_i + c_{z,i} + d_{z,i} v_i^2 + e_{z,i} v_i) \end{pmatrix} \text{ (equation1)},$$

where x_p, y_p, and z_p are the predicted target positions in the left-right, cranio-caudal, and anterior-posterior directions, n is the number of IR markers, and s and v are the predicted position and velocity of each IR marker in the anterior-posterior direction. The positions of the IR markers are predicted from the past motion to compensate for DTT system delay. Parameters of the 4D model (*a*, *b*, *c*, *d*, and *e*) were optimised using a least-squares algorithm so that residual errors between the P_p and P_d were minimised.

During beam delivery, the future 3D target position is predicted from the displacements of the IR markers using the 4D model, and then the corresponding tracking angle is transferred continuously to the gimballed x-ray head.

Tracked target position calculated from the tracking angle of the gimballed x-ray head

Intrafractional tracking accuracy was assessed by the detected target position (P_d) from the fluoroscopic images and the corresponding predicted target position (P_p) and the tracked target position, calculated from the synchronously acquired log files. The tracked target position was derived from an intersection of a tracking orientation of the gimballed x-ray head with a tracked tumour plane. The tracked tumour plane was defined as the perpendicular plane to the gimbal angle of 0° for each port at the depth of the moving tumour. The tracked target position, based on P_d ($P_{t,d}$), was calculated in the following three steps:

(1) Conversion of P_d from room to gantry-ring coordinates:

$$\begin{pmatrix} u_d \\ v_d \\ w_d \end{pmatrix} = \begin{pmatrix} \cos G \cos R & -\cos G \sin R & -\sin G \\ -\sin R & -\cos R & 0 \\ \sin G \cos R & -\sin G \sin R & \cos G \end{pmatrix} \cdot \begin{pmatrix} x_d \\ y_d \\ z_d \end{pmatrix} \quad \text{(equation 2)},$$

where x_d, y_d, and z_d are the detected target positions along the LR, the CC, and the AP directions in room coordinates, and G and R are the gantry and ring angle, and u_d, v_d, and w_d (units: mm) are the detected target positions in gantry-ring coordinates corresponding to x_d, y_d, and z_d.

(2) Calculation of $P_{t,d}$ at the depth of P_d in gantry-ring coordinates

$$\begin{pmatrix} u_{t,d} \\ v_{t,d} \\ w_{t,d} \end{pmatrix} = \begin{pmatrix} (960 - w_d)\tan\theta_P \\ (960 - w_d)\tan\theta_T \\ w_d \end{pmatrix} \quad \text{(equation 3)},$$

where $u_{t,d}$, $v_{t,d}$, and $w_{t,d}$ (units: mm) are the tracked target positions in gantry-ring coordinates at the depth of the detected target position ($w_{t,d}$). θ_P and θ_T are the pan and tilt angle of the gimballed x-ray head, and 960 mm is the distance from the rotation centre of the gimballed x-ray head to the isocentre.

(3) Conversion of $P_{t,d}$ from gantry-ring to room coordinates:

$$\begin{pmatrix} x_{t,d} \\ y_{t,d} \\ z_{t,d} \end{pmatrix} = \begin{pmatrix} \cos G \cos R & -\sin R & \sin G \cos R \\ -\cos G \sin R & -\cos R & -\sin G \sin R \\ -\sin G & 0 & \cos G \end{pmatrix} \cdot \begin{pmatrix} u_{t,d} \\ v_{t,d} \\ w_{t,d} \end{pmatrix} \text{ (equation 4)},$$

where $x_{t,d}$, $y_{t,d}$, and $z_{t,d}$ (units: mm) are the tracked target positions in room coordinates. The tracked target position, based on P_p ($P_{t,p}$), at the depth of the predicted target position (w_p) was calculated similarly.

Intrafractional mechanical (iE_M), prediction (iE_P), and overall targeting errors (iE_T) were defined as follows:

$$iE_M = \begin{pmatrix} x_{t,p} \\ y_{t,p} \\ z_{t,p} \end{pmatrix} - \begin{pmatrix} x_p \\ y_p \\ z_p \end{pmatrix} \text{ (equation 5)},$$

$$iE_P = \begin{pmatrix} x_p \\ y_p \\ z_p \end{pmatrix} - \begin{pmatrix} x_d \\ y_d \\ z_d \end{pmatrix} \text{ (equation 6)},$$

$$iE_T = \begin{pmatrix} x_{t,d} \\ y_{t,d} \\ z_{t,d} \end{pmatrix} - \begin{pmatrix} x_d \\ y_d \\ z_d \end{pmatrix} \text{ (equation 7)},$$

where $x_{t,p}$, $y_{t,p}$, and $z_{t,p}$ (units: mm) are the tracked target positions at the depth of the P_p used for the verification of the mechanical error of the gimballed x-ray head against the predicted target positions, and x_p, y_p, and z_p (units: mm) are the predicted target positions used as the tracking commands to the gimballed x-ray head, and x_d, y_d, and z_d (units: mm) are the detected target positions, and $x_{t,d}$, $y_{t,d}$, and $z_{t,d}$ (units: mm) are the tracked target positions at the depth of the P_d used for the verification of the overall targeting error of the gimballed x-ray head against the moving tumour.

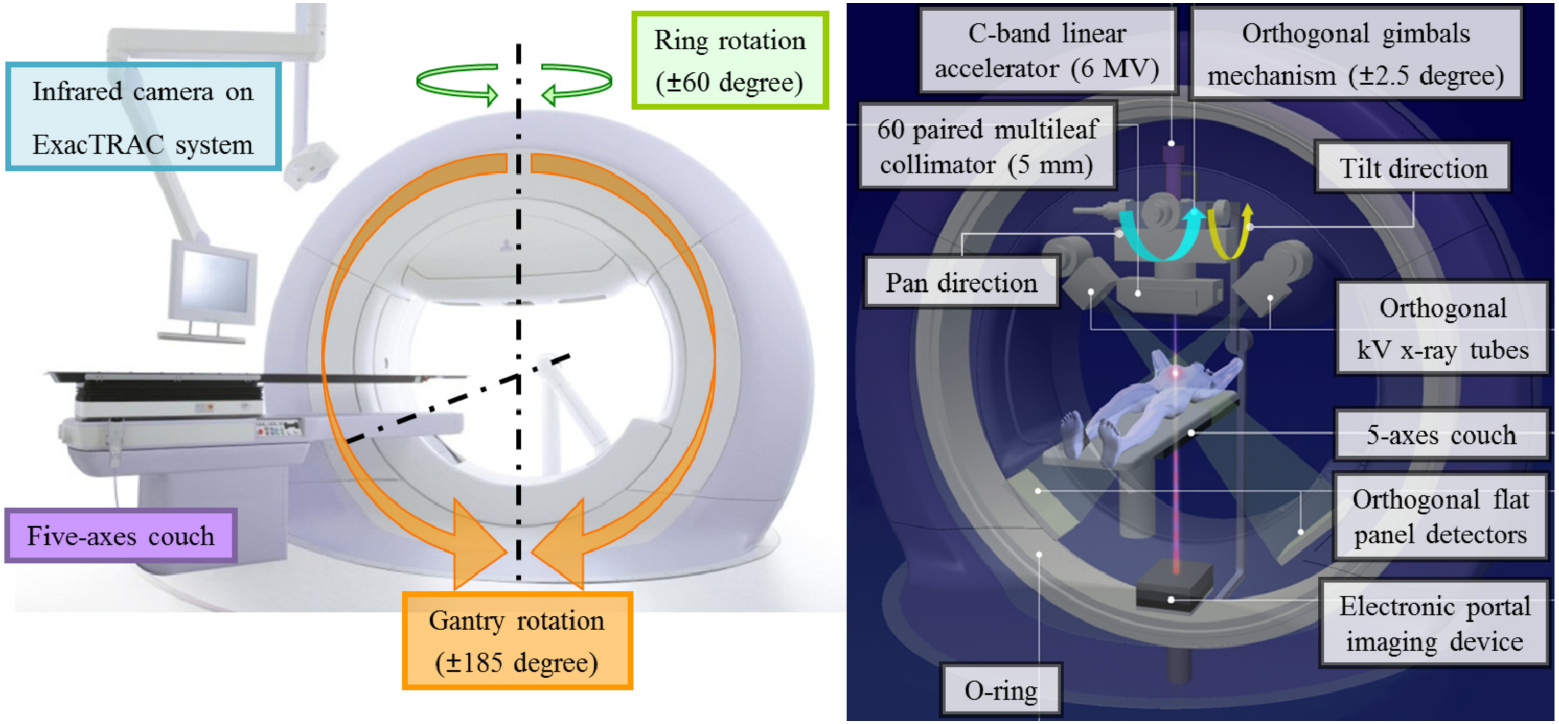

65

66 **Supplementary Figure 1**. Schematic diagram of the Vero4DRT system.

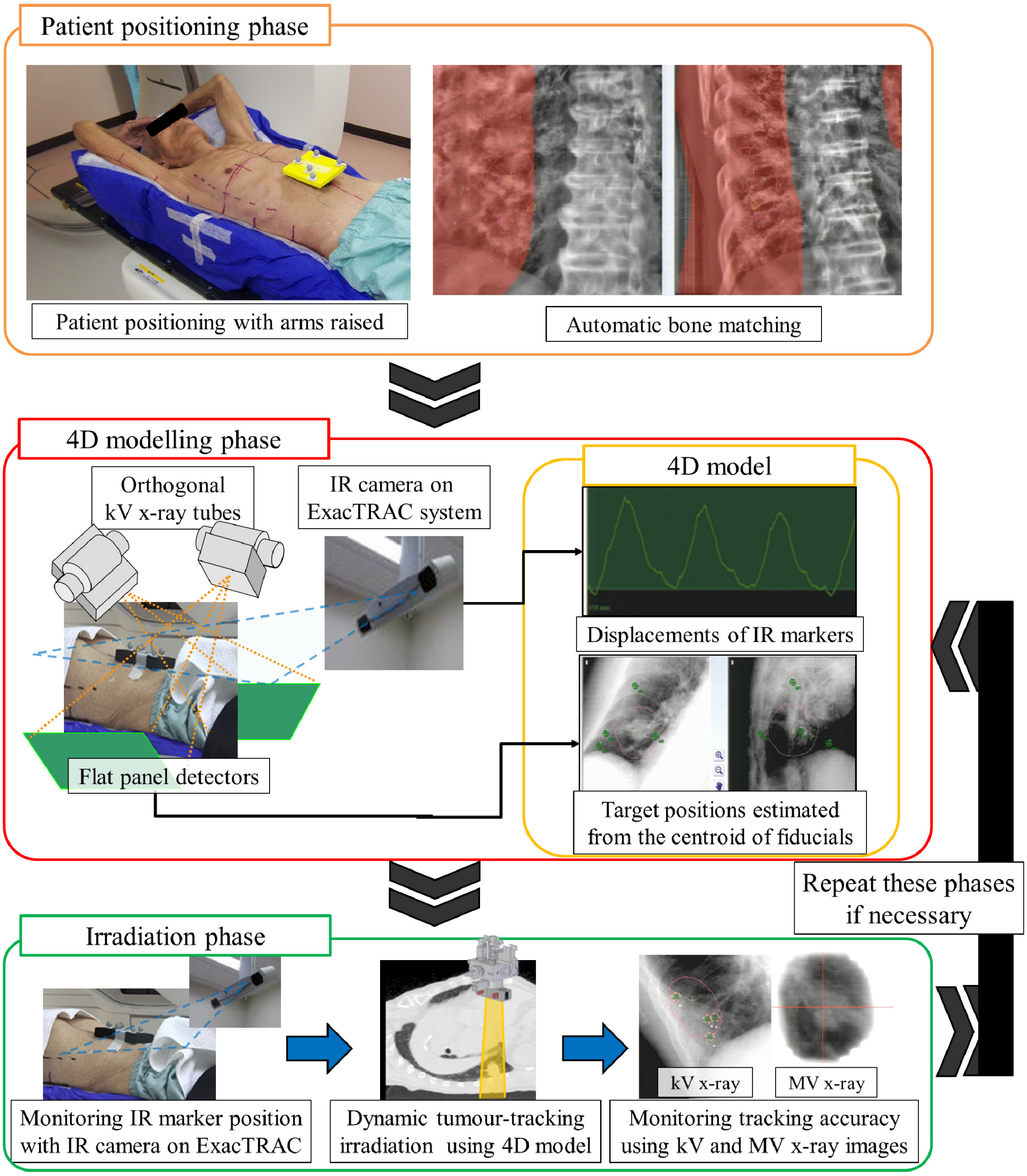

67

68 **Supplementary Figure 2**. Infrared (IR) marker-based hybrid dynamic tumour tracking
69 irradiation ("IR Tracking") procedure.

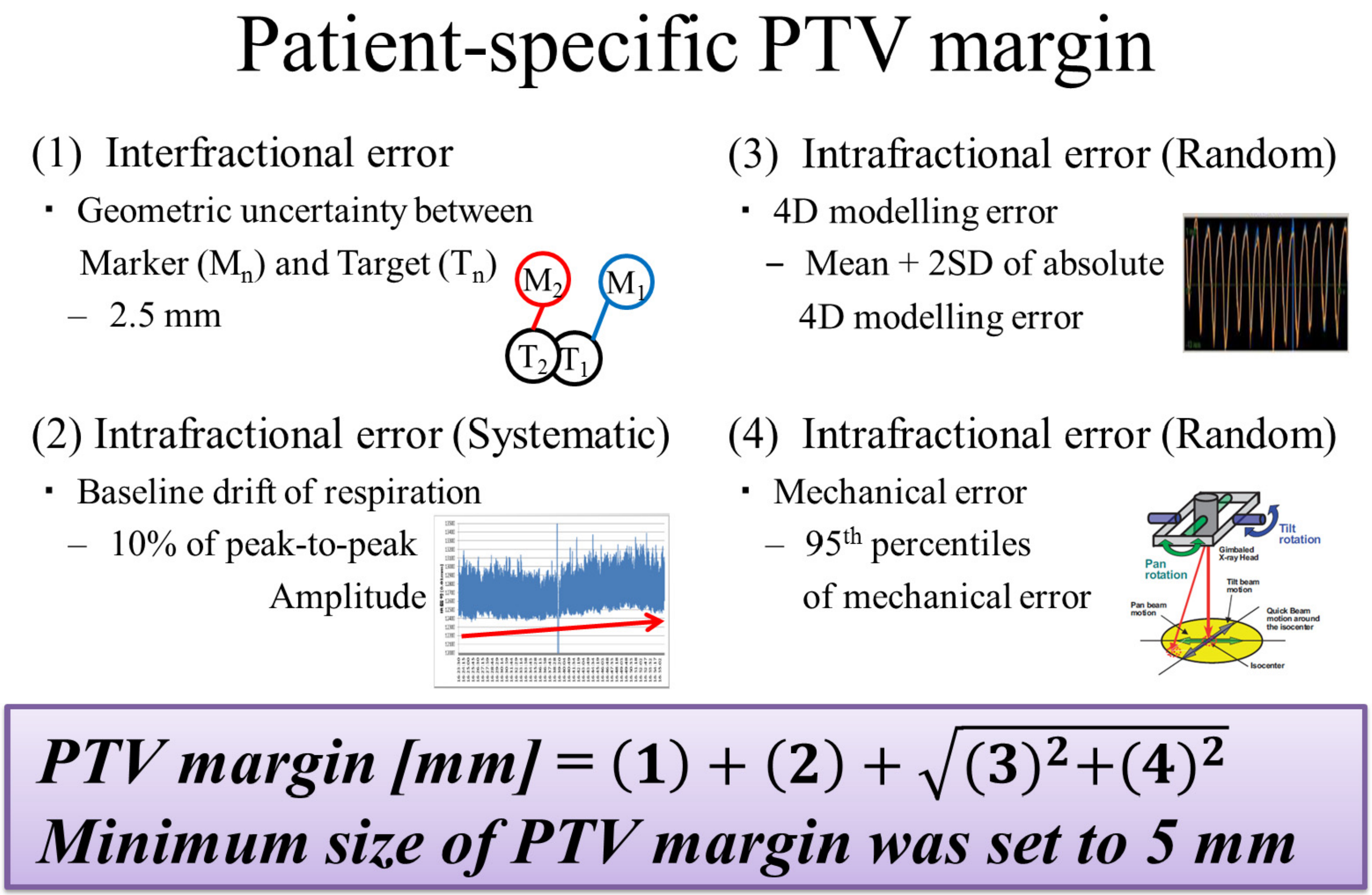

Supplementary Figure 3. Definition of the patient-specific planning target volume (PTV) margin.

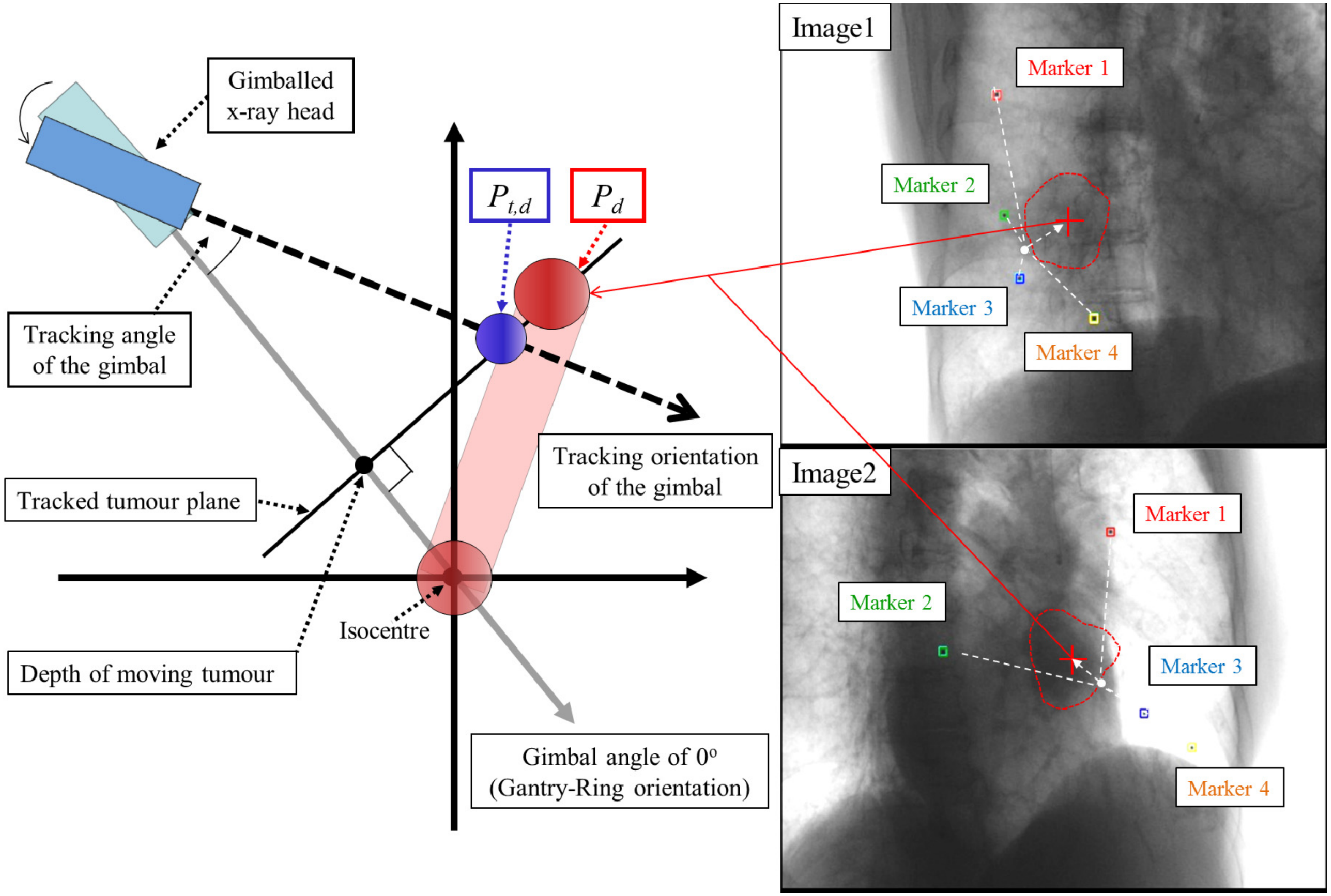

72

73 **Supplementary Figure 4.** The geometric point of the tracked target position ($P_{t,d}$) based on the detected target position (P_d)

74 calculated from orthogonal fluoroscopic images and synchronously acquired log files.

Supplementary Figure 5. Screen shot of the Vero4DRT system during creation of the prediction model ("4D model"). The right four groups of waves, from top to bottom, show variations in the infrared (IR) markers' positions in the anterior-posterior direction and the target positions in the lateral, craniocaudal, and anterior-posterior directions, respectively. In the graphs of the target position, dark-coloured waves show the detected target position and light-coloured waves show the predicted target position.